

Effects of Zinc Binding on the Structure and Dynamics of the Intrinsically Disordered Protein Prothymosin α : Evidence for Metalation as an Entropic Switch[†]

Shiluan Yi,[‡] Brian L. Boys,[§] Anne Brickenden,[‡] Lars Konermann,^{‡,§} and Wing-Yiu Choy^{*,‡,§}

Departments of Biochemistry and Chemistry, The University of Western Ontario, London, Ontario, Canada N6A 5C1

Received July 25, 2007; Revised Manuscript Received September 4, 2007

ABSTRACT: Prothymosin α (ProT α) is a small acidic protein that is highly conserved among mammals. The human form has 110 amino acid residues (M.W. 12.1 kDa; pI \sim 3.5) and is found to be expressed in a wide variety of tissues. ProT α plays an essential role in cell proliferation and apoptosis, and it is involved in transcriptional regulation of oxidative stress-protecting genes. Despite the multiple biological functions ProT α has, the protein does not adopt a well-defined three-dimensional structure under physiological conditions. Previous studies have shown that the interaction between ProT α and some of its protein targets is significantly enhanced in the presence of zinc ions, suggesting that zinc binding plays a crucial role in the protein's function. In this work, we use nuclear magnetic resonance spectroscopy and electrospray ionization mass spectrometry to characterize the structure and dynamics of ProT α and its complexation with Zn²⁺. We found that zinc binding causes partial folding of the C-terminal half of ProT α , especially the Glu-rich region, while the N-terminal portion of the protein remains largely unstructured. The metalated protein also exhibits a significantly reduced flexibility. ProT α shows a high specificity for Zn²⁺, and the interactions with other divalent cations (Ca²⁺, Mg²⁺) are much weaker. On the basis of the site-specific information obtained here, as well as the results from previous studies, we propose that the conformational and dynamic changes upon zinc binding may act as an entropic switch that greatly facilitates the binding to other proteins.

The function of proteins is usually linked to the presence of a well-defined native conformation. However, in recent years an increasing number of proteins has been identified as being intrinsically unstructured, yet still biologically functional (1–3). Importantly, many of these disordered proteins are found to perform crucial regulatory functions (1, 4, 5). Concurrent with these experimental findings, bioinformatics studies have also predicted that a significant fraction of proteins in various organisms (over 30% in human) are either completely disordered or contain long disordered regions (2, 6). In particular, this includes proteins that are involved in transcriptional regulation, cell signaling, or associated with cancers and cardiovascular diseases (7–9). Knowledge of how these disordered proteins function on a structural basis will facilitate the design of drugs and the development of novel therapeutic approaches (10).

Unraveling the structure–function relationship of disordered proteins is an extremely challenging task (11–15). Unlike globular folded proteins, intrinsically disordered proteins lack specific tertiary structure under native conditions and exist as ensembles of conformers that undergo fast

interconversion (13, 16). Despite the fact that disordered proteins exhibit a high degree of flexibility, they often do not represent genuine random coils; instead, many of them show significant conformational propensities. Interestingly, protein segments with a significant amount of residual structure are frequently found to act as molecular recognition elements (MoREs)¹ for target binding (17, 18). Some disordered proteins contain multiple distinct MoREs along their sequence (18–20), thereby allowing the interaction with a diversity of targets. This feature may explain why many hub proteins in protein interaction networks are intrinsically disordered (21). Alternatively, rapid conformational changes may also allow a single binding site to interact with several different proteins (22).

The characterization of residual structured elements in disordered proteins can provide important insights into the function of these species. Unfortunately, the lack of a well-defined tertiary fold precludes the use of many conventional experimental techniques (11–13). Since intrinsically disordered proteins do not crystallize, nuclear magnetic resonance (NMR) spectroscopy remains the only other technique that can be used for obtaining structural information at the atomic level. With recent advances in technology and methodology,

[†] This work was supported by the Canadian Institutes of Health Research (CIHR), the Natural Sciences and Engineering Research Council of Canada (NSERC), the Canada Foundation for Innovation (CFI), the Province of Ontario, and the Canada Research Chairs Program. W.Y.C. is the recipient of a CIHR New Investigator Award and an Ontario Early Researcher Award.

* To whom correspondence should be addressed. Tel: (519) 661-3161. Fax: (519) 661-3175. E-mail: jchoy4@uwo.ca.

[‡] Department of Biochemistry.

[§] Department of Chemistry.

¹ Abbreviations: CBP, CREB-binding protein; CD, circular dichroism; ESI-MS, electrospray ionization mass spectrometry; GRR, Glu-rich region; Keap1, Kelch-like ECH-associated protein 1; MoRE, molecular recognition element; NMR, nuclear magnetic resonance; NOE, nuclear Overhauser effect; Nrf2, nuclear factor E2-related factor 2; PFG-NMR, pulsed-field gradient NMR; ProT α , Prothymosin α ; R_1 , longitudinal relaxation rate; $R_{1\rho}$, relaxation rate in rotating frame; R_2 , transverse relaxation rate.

conformational propensity and transient interactions present in disordered proteins can now be probed by various NMR techniques (13, 23–27). Several recent studies have demonstrated the power of these approaches for scrutinizing the molecular mechanisms by which disordered proteins interact with their targets (13, 23–27).

Prothymosin α (ProT α) is a small, acidic protein that is highly conserved among mammals (28–30). The ubiquitous expression of this protein in a wide variety of tissues suggests that it plays an essential biological role. Previous studies have demonstrated that ProT α is involved in cell proliferation (29–31). It was shown that ProT α binds to the linker histone H1 and modulates the interaction of H1 with chromatin, suggesting that the protein may play a role in chromatin remodeling (32, 33). There is also evidence linking ProT α to transcriptional regulation. For instance, the protein has been reported to interact with CREB-binding protein (CBP), and it enhances the transactivation activity of CBP (34, 35). It has also been shown that ProT α is involved in regulating the expression of oxidative stress-protecting genes (36). Nuclear factor E2-related factor 2 (Nrf2) is a key protein that coordinates the cellular response to oxidative stress (37). Its transcriptional activity is negatively regulated by the inhibitor Kelch-like ECH-associated protein 1 (Keap1), which interacts with Nrf2 and targets it for the degradation by the proteasome (38). By competing with Nrf2 for binding to Keap1 in the nucleus, ProT α has been shown to up-regulate the Nrf2-dependent cytoprotective genes (36).

ProT α is also thought to be involved in other important processes. In the intrinsic pathway of programmed cell death, apoptotic stimuli result in the release of cytochrome *c* from mitochondria into the cytosol (39, 40). The released cytochrome *c* binds to apoptotic protease-activating factor 1 (Apaf-1) and dATP to form the apoptosome (41–44), which in turn activates a cascade of caspases. These caspases cleave a variety of protein targets and eventually lead to cell death. ProT α plays a central role in apoptosis by blocking the formation of the apoptosome (45, 46). The details of this molecular mechanism, however, have not been elucidated yet.

Previous structural studies have demonstrated that human ProT α is intrinsically disordered under physiological conditions (47, 48). The primary structure of this protein is highly unusual (29). Forty-eight percent of its sequence is composed of acidic residues (34 Glu and 19 Asp), and interestingly, the protein does not contain any aromatic amino acids. Hydrophobic residues, such as valine, leucine and isoleucine, are unevenly distributed in the sequence, with most of them being located within the first 24 amino acids from the N-terminus. The high net charge and low overall hydrophobicity may explain why this protein does not adopt a stable conformation under physiological conditions (49).

The disordered nature of ProT α appears to be the key for understanding its promiscuous binding behavior since the entire primary structure can be accessible, and discrete parts of the protein may be involved in interactions with different targets (29). Intriguingly, the binding of ProT α to several targets such as Keap1 (36), cytochrome *c* (46), and Rev (50) has been shown to be mediated by zinc. To gain a better understanding of the Zn²⁺–ProT α interactions, in this work, we employed NMR spectroscopy and electrospray ionization mass spectrometry (ESI-MS) to characterize changes in the

structure and dynamics of ProT α upon zinc binding. Our results show that Zn²⁺ specifically interacts with the C-terminal portion of ProT α , causing it to undergo partial folding, while the N-terminal part (residues 1–40) remains highly flexible. The potential implications of these conformational and dynamic changes for the binding of ProT α to its target proteins are discussed.

MATERIALS AND METHODS

Expression and Purification of Recombinant ProT α . The pHP12A plasmid carrying the human ProT α cDNA was kindly supplied by Dr. Vartapetian at the Moscow State University (Russia) (51). The detailed protocol for protein expression and purification has been reported elsewhere (52). Briefly, the protein was expressed in *E. coli* BL21(DE3) cells (Novagen). For uniformly ¹⁵N/¹³C-labeled protein samples, cells were grown in M9 minimal medium containing ¹⁵NH₄-Cl (Cambridge Isotope Laboratories) and ¹³C₆-D-glucose (Isotec) as the sole nitrogen and carbon sources, respectively. The extraction and prepurification of ProT α was based on a heat-cooling protocol previously described by Kalthoff (53) with modifications. By combining this method with ammonium sulfate precipitation and anion exchange chromatography, approximately 20 mg of ProT α with high purity was obtained from a 1 L media culture.

NMR Spectroscopy. NMR experiments described below, unless stated otherwise, were performed at 22 °C on a Varian Inova 600 MHz spectrometer equipped with an xyz-gradient triple resonance probe, in the presence of 40 mM HEPES (pH 7.0) with 10% (v/v) D₂O (Cambridge Isotope Laboratories). One millimolar sodium 2,2-dimethyl-2-silapentane-5-sulfonate (DSS, Sigma) was added to each NMR sample as internal standard for chemical shift referencing (54). All data sets were processed using NMRPipe (55), and the spectra were analyzed with NMRView (56). For the backbone resonance assignment, a set of five heteronuclear triple-resonance experiments, HNCACB, CBCA(CO)NH, CCC-TOCSY, HNCACO, and HNCO, were recorded using a concentration of 0.6 mM for the ¹³C/¹⁵N-labeled protein sample (57).

For zinc titration experiments, ¹H-¹⁵N HSQC spectra of 0.1 mM ¹⁵N-labeled ProT α were recorded in the presence of different concentrations of ZnCl₂ (0–3 mM). The composite chemical shift changes ($\Delta\delta_{\text{comp}}$) of ProT α upon the addition of Zn²⁺ were calculated according to $\Delta\delta_{\text{comp}} = [(\Delta\delta^1\text{H}_N)^2 + (\Delta\delta^{15}\text{N})^2]^{1/2}$, where $\Delta\delta^1\text{H}_N$ and $\Delta\delta^{15}\text{N}$ are the changes in ¹H_N and ¹⁵N chemical shifts (in Hz) upon the addition of zinc. To probe the changes of ¹³C $_{\alpha}$ and ¹³C $_{\beta}$ chemical shifts upon Zn²⁺ binding, HNCACB and CBCA(CO)NH spectra of 0.3 mM ¹³C/¹⁵N-labeled ProT α were acquired in the presence of 6 mM ZnCl₂.

Pulsed-field gradient (PFG) NMR diffusion measurements were performed using the water-suppressed longitudinal encode–decode (water-sLED) pulse sequence (58) on a sample with 0.1 mM unlabeled ProT α . Nine millimolar 1,4-dioxane was added to the protein sample as a reference molecule for the subsequent hydrodynamic radius (*R_h*) calculation (59). Thirteen different gradient strengths (*G*) were used, with the strongest gradient leading to about 60% decay in the protein signals. Intensities (*I*) of the signals from protein and dioxane were then fitted to the expression, $I(G)$

= $A\exp(-DG^2)$, where D is the signal decay rate, which is proportional to the translational diffusion coefficient (59). On the basis of the X-ray structure of dioxane, R_h of this molecule was determined to be 2.12 Å (59). R_h values for ProTα were then determined on the basis of the decay rates of the protein ($D_{protein}$) and the dioxane ($D_{dioxane}$) signals, using the equation $R_h(\text{protein}) = (D_{dioxane}/D_{protein}) \times 2.12 \text{ Å}$ (59). The experiment was repeated twice; three different signals in the aliphatic region of the protein were selected for the R_h calculation.

Backbone ^{15}N R_1 , $R_{1\rho}$, and steady-state ^1H - ^{15}N NOE experiments (60, 61) were carried out using a 0.3 mM ^{15}N -labeled ProTα sample in the presence and absence of 6 mM ZnCl_2 . All R_1 , $R_{1\rho}$, and ^1H - ^{15}N NOE spectra were recorded using 128×512 complex points in the t_1 and t_2 dimensions and spectral widths of 8000 and 1154 Hz for ^1H (F_2) and ^{15}N (F_1), respectively. R_1 experiments were performed with various delay times between 10 and 640 ms. For $R_{1\rho}$ measurements, delay times ranging from 10 to 150 ms were used. The R_1 and $R_{1\rho}$ relaxation rates of each assigned residue with well-resolved signals were determined by fitting the measured peak intensities at different relaxation delay times, $I(t)$, to a two-parameter exponential decay curve $I(t) = I_0 \exp(-Rt)$, where I_0 is the initial peak intensity at $t = 0$, and R is the calculated ^{15}N relaxation rate constant. Errors of the relaxation rates were estimated on the basis of the fits of the data to the decay curves. Duplicate measurements were used to verify the error estimated. The ^{15}N R_2 value was then calculated on the basis of the observed R_1 , $R_{1\rho}$, offset between the resonance and the carrier frequency ($\Delta\omega$) in Hz, and the spin-lock RF field ($B_{SL} = 1.5 \text{ kHz}$), where $R_{1\rho} = R_1 \cos^2\theta + R_2 \sin^2\theta$, with $\tan \theta = B_{SL}/\Delta\omega$ (62).

Steady-state ^1H - ^{15}N NOE values were determined from spectra recorded in the presence and the absence of ^1H saturation. For the ^1H - ^{15}N NOE spectrum recorded with proton saturation, a 7 s delay between scans followed by a 5 s period of saturation were used. For the spectrum recorded without saturation, a 12 s delay between scans was used. The values of heteronuclear NOEs were obtained from the ratios of peak intensities in the spectra recorded with and without ^1H saturation. Errors were estimated on the basis of the signal-to-noise ratios of the individual peaks.

Reduced Spectral Density Analysis. Values of the spectral density function were calculated on the basis of the measured relaxation parameters using the method proposed by Farrow et al. (63). Briefly, the high-frequency spectral density terms, $J(\omega_H \pm \omega_N)$ and $J(\omega_H)$, which contribute to the ^{15}N spin relaxation processes, are assumed to have approximately equal magnitudes. Under this assumption, the R_1 , R_2 , and steady-state NOE can be described by the following equations:

$$R_1 = \left(\frac{d^2}{4}\right) [3J(\omega_N) + 7J(0.921\omega_H)] + c^2J(\omega_N) \quad (1)$$

$$R_2 = \left(\frac{d^2}{8}\right) [4J(0) + 3J(\omega_N) + 13J(0.955\omega_H)] + \left(\frac{c^2}{6}\right) [3J(\omega_N) + 4J(0)] \quad (2)$$

$$\text{NOE} = 1 + \left(\frac{d^2}{4R_1}\right) \left(\frac{\gamma_H}{\gamma_N}\right) [5J(0.87\omega_H)] \quad (3)$$

where $d = \mu_0 h \gamma_H \gamma_N / [(8\pi^2) r_{NH}^3]$, $c = (\omega_N / \sqrt{3}) \Delta$, μ_0 is the permeability of free space, h is the Planck's constant, γ_H and γ_N are the gyromagnetic ratios of ^1H and ^{15}N , respectively, r_{NH} is the amide bond length (1.02 Å), and Δ is the difference between the parallel and perpendicular components of the axially symmetric ^{15}N chemical shift tensor (-170 ppm). The value of $J(0.87\omega_H)$ was determined from eq 3. $J(0.921\omega_H)$ and $J(0.955\omega_H)$ were then obtained from the value of $J(0.87\omega_H)$ by assuming that $J(\omega) \propto \omega^{-2}$ at $\omega \approx \omega_H$ (63). $J(0)$ and $J(\omega_N)$ were then determined from eqs 1 and 2. Uncertainties in the spectral densities were obtained using a Monte Carlo procedure based on the estimated errors of the relaxation parameters.

Electrospray Ionization Mass Spectrometry. Mass spectra were recorded on a Q-TOF Ultima API (Waters/Micromass, Manchester, UK), utilizing a standard Z-spray ESI source operating in positive ion mode at 3.5 kV. All mass spectra were acquired in the presence of 150 mM ammonium acetate at pH 6.8. The protein concentration was 0.1 mM to ensure consistency with the NMR experiments. A cone voltage of 45 V, and RF lens 1 voltage of 20 V were found to be optimal. The desolvation and source temperatures were 100 °C and 80 °C, respectively. Mass calibration was performed with CsI. The ion optics were adjusted to provide uniform transmission in the m/z range of interest. All data were acquired and analyzed using MassLynx software provided by the instrument manufacturer.

To reduce salt interferences during ESI (64), solutions containing 0.1 mM ProTα and 3 mM zinc, calcium, or magnesium chloride were subjected to on-line desalting immediately prior to injection into the ion source. The homemade microdialysis device used for this purpose employed a counter-current flow design previously described in the literature (65). Briefly, the microdialyzer consisted of a 200 $\mu\text{m} \times 15 \text{ cm}$ regenerated cellulose hollow dialysis fiber (nominal MWCO 13 kDa, Spectrum, CA) inside a 1 mm i.d. PEEK tube. The ends of the apparatus were sealed by means of PEEK T-unions (Upchurch Scientific). Samples were infused through the microdialyzer into the mass spectrometer at a flow rate of 2 $\mu\text{L min}^{-1}$ via a syringe pump. A counter flow of 150 mM ammonium acetate solution was pumped through the outer peak tube at a rate of 9 mL min^{-1} . Spectroscopic control experiments on potassium permanganate showed a 220-fold reduction in salt concentration at the exit of the inner fiber. Under these conditions, the average residence time of the protein inside the device was 140 s, with an additional 50 s for transferring the solution to the outlet of the ESI source.

Circular Dichroism (CD) Spectropolarimetry. CD experiments were performed on a Jasco J-810 spectropolarimeter (Easton, MD), equipped with a PTC-423S Peltier temperature control unit, using a cuvette with 0.1 mm path length. Spectra of 0.1 mM ProTα (in 10 mM HEPES and 150 mM NaCl, at pH 7.0) were recorded at 22 °C in the absence and presence of 3 mM of ZnCl_2 , CaCl_2 , or MgCl_2 . The data were converted to mean residue ellipticity (θ) by standard procedures using the software supplied by the manufacturer.

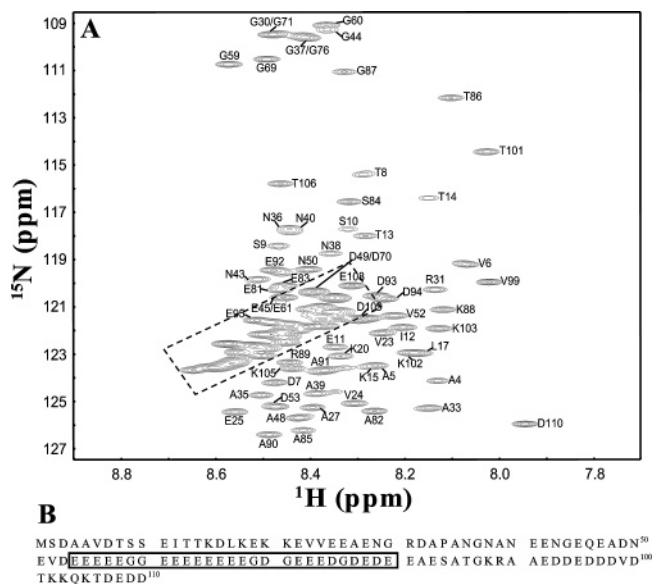


FIGURE 1: Backbone resonance assignments of ProTα. (A) Two-dimensional ^1H - ^{15}N HSQC spectrum. The dashed box indicates an acidic residue-rich region that could not be assigned. (B) Protein sequence of ProTα. The boxed region indicates the glutamic acid-rich region (GRR).

RESULTS

Backbone NMR Resonance Assignments. Five heteronuclear triple-resonance experiments, HNCACB, CBCA(CO)NH, CCC-TOCSY, HNCACO, and HNCO, were used to assign the backbone $^1\text{H}_\text{N}$, ^{15}N , $^{13}\text{C}_\alpha$, $^{13}\text{C}_\beta$, and ^{13}CO resonance signals of ProTα. Figure 1A shows the ^1H - ^{15}N HSQC spectrum of the protein. The narrow dispersion of the backbone amide proton chemical shifts (7.9–8.7 ppm) reflects the fact that ProTα is unstructured under the nondenaturing conditions used, thus confirming the intrinsically disordered nature of this protein (47). Because of considerable signal overlap and the highly degenerate amino acid sequence, sequential resonance assignment was challenging. A total of 66 amide signals (out of 109 non-proline residues) could be assigned. Thirty-six of the 43 unassigned amino acids are acidic residues (25 Glu and 11 Asp), all of which have their signals crowded in a narrow region of the HSQC spectrum (dashed region of Figure 1A). Since 56% of the unassigned acidic residues are located in the glutamic acid-rich region (GRR, residues 54–80, highlighted in Figure 1B), spectral changes in this crowded region are strong indicators of structural alterations in the GRR, as discussed in more detail below.

Even though the backbone resonances could not be completely assigned, it is still possible to derive valuable structural information from the assigned residues. $^{13}\text{C}_\alpha$ and $^{13}\text{C}_\beta$ chemical shifts report on the backbone geometry, exhibiting values that deviate systematically from those expected for a random coil when the residue is located within a secondary structure element. The average secondary $^{13}\text{C}_\alpha$ ($^{13}\text{C}_\beta$) shifts are 3.1 (−0.4) and −1.5 (2.2) ppm for stable α -helical and β -strand conformations, respectively (66, 67). In this work, we have used $(\Delta\delta^{13}\text{C}_\alpha - \Delta\delta^{13}\text{C}_\beta)$ as a reference-independent measure of the residue-specific secondary structure propensity, where $\Delta\delta^{13}\text{C}_\alpha$ and $\Delta\delta^{13}\text{C}_\beta$ are the deviations of $^{13}\text{C}_\alpha$ and $^{13}\text{C}_\beta$ chemical shifts from the predicted random coil values, respectively (67, 68). Figure

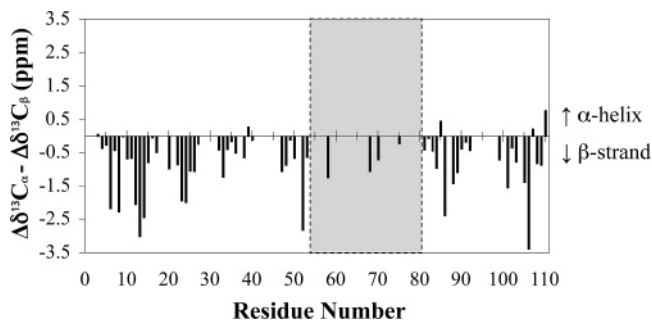


FIGURE 2: Reference-independent $(\Delta\delta^{13}\text{C}_\alpha - \Delta\delta^{13}\text{C}_\beta)$ secondary chemical shifts of ProTα. Positive and negative values indicate the helical and β -strand propensities, respectively. The shaded box indicates the GRR, which contains 20 unassigned acidic amino acid residues.

2 shows a plot of $(\Delta\delta^{13}\text{C}_\alpha - \Delta\delta^{13}\text{C}_\beta)$ versus residue number. The small but systematic deviations indicate that unlike many other intrinsically disordered proteins, ProTα displays no helical propensity along the sequence, but instead, a large portion of the protein shows slight β -strand propensity or adopts extended structure.

Chemical Shift Changes upon Zinc Binding. The structural response of 0.1 mM ^{15}N -labeled ProTα upon addition of 3 mM ZnCl_2 was monitored by ^1H - ^{15}N HSQC experiments (Figure 3A). Changes in the composite chemical shift, $\Delta\delta_{\text{comp}}$, of $^1\text{H}_\text{N}$ and ^{15}N for the assigned residues upon addition of Zn^{2+} were determined as defined in the Materials and Methods section (Figure 3B). The large chemical shift changes clearly demonstrate that metal binding induces significant conformational changes. Notably, the data in Figure 3B reveal that the zinc-binding site(s) are located in the C-terminal half of the protein since none of the assigned residues in the first 40 amino acids from the N-terminus shows major chemical shift changes. On the basis of the spectral changes in the dashed region of Figure 3A, it can be estimated that the $\Delta\delta_{\text{comp}}$ values for the Glu/Asp from residues 54–80 are likely in the range of 85 Hz, even though most of the Glu/Asp residues in the GRR could not be unambiguously assigned. To probe the change in secondary structure propensity of ProTα upon zinc binding, the $^{13}\text{C}_\alpha$ and $^{13}\text{C}_\beta$ chemical shifts of the protein in the absence and presence of Zn^{2+} were compared (Figures 2 and 3C). The results show that there is an increase in helical propensity for residues 48–83 upon binding to Zn^{2+} .

To investigate the specificity of zinc binding to ProTα, titration experiments analogous to those in Figure 3A and B were repeated in the presence of 150 mM NaCl and with other divalent cations. Figure 4 shows the spectral changes observed upon the addition of 3 mM of ZnCl_2 , CaCl_2 , and MgCl_2 . In the presence of 150 mM NaCl, the addition of Zn^{2+} (blue; Figure 4A and B) to ProTα leads to chemical shift changes qualitatively similar to those in Figure 3A, B. In contrast, the spectral alterations caused by the presence of Ca^{2+} (green; Figure 4C and D) and Mg^{2+} (black; Figure 4E and F) are almost 1 order of magnitude smaller. These results clearly show that Zn^{2+} , but not Ca^{2+} or Mg^{2+} , interact specifically with the C-terminal portion of ProTα even at high ionic strength.

Mass Spectrometry and Circular Dichroism Spectroscopy. ESI-MS was employed to verify the specificity of Zn^{2+} binding to ProTα in the presence of 150 mM ammonium

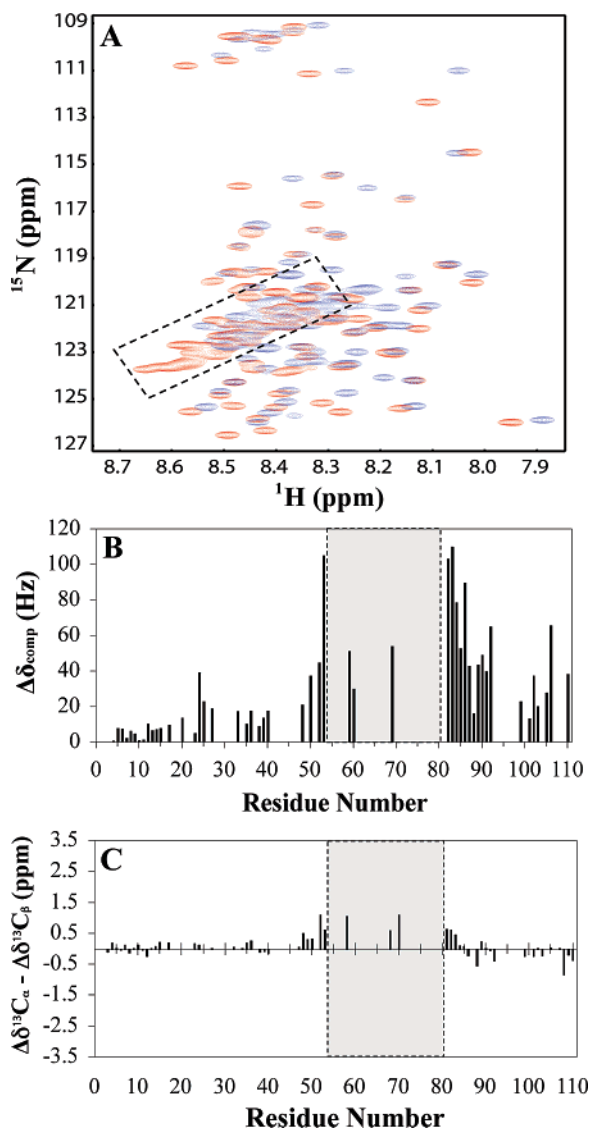


FIGURE 3: (A) ^1H - ^{15}N HSQC spectra of ProT α in the absence (red) and presence (blue) of 3 mM of Zn^{2+} . (B) Composite $^1\text{H}_\text{N}$ and ^{15}N chemical shift changes (in Hz), $\Delta\delta_{\text{comp}}$, of ProT α upon the addition of 3 mM of Zn^{2+} . (C) Plot of $(\Delta\delta^{13}\text{C}_\alpha - \Delta\delta^{13}\text{C}_\beta)$ vs residue number in the presence of 6 mM of Zn^{2+} . The shaded boxes in (B) and (C) indicate the GRR.

acetate. Initial experiments using 0.1 mM protein and 3 mM ZnCl_2 , CaCl_2 , or MgCl_2 resulted in spectra with unacceptable signal-to-noise ratios. This effect is ascribed to the well-known interference of metal cations with the ESI process (64). Lowering the metal concentrations to 0.6 mM improved the quality of the spectra but resulted in low binding levels, with only a slight preference for zinc (data not shown). We therefore chose a strategy where 0.1 mM protein aliquots were exposed to metal cations at a concentration of 3 mM. The metal concentration was then rapidly decreased by microdialysis to about 14 μM immediately prior to injection into the mass spectrometer. The rationale behind this strategy was that differences in binding should persist, assuming that dissociation of the metal–protein complexes does not go to completion during the ca. 3 min desalting step.

Control experiments conducted in the absence of divalent cations (Figure 5A) revealed a bimodal charge state distribution for ProT α , resembling data previously obtained for globular proteins under semi-denaturing conditions (69–72).

The more highly charged ions of ProT α (around 15+) represent extensively unfolded solution conformers, whereas the low charge states (7+ and 8+) are assigned to more compact species (73, 74). This charge state distribution, therefore, is consistent with the presence of a highly heterogeneous mixture of different solution-phase conformers. Unfortunately, extracting quantitative information on the relative concentrations of the various species from these data is not straightforward (75, 76). Charge-state distributions similar to that in Figure 5A were observed following metal incubation and microdialysis. Most importantly, the residual binding level for Zn^{2+} is higher than those for the other two divalent cations by at least a factor of 3 (Figure 5B–D). The ESI-MS data suggest that the compact conformers of ProT α associate with Zn^{2+} more strongly than their disordered counterparts. This is seen in the expanded partial spectra of Figure 5B, where the folded conformation (7+) associates with up to five Zn^{2+} ions, whereas the unfolded conformation (15+) binds no more than two. One should be careful not to extrapolate from these ESI-MS data to the number of bound metal ions in solution for several reasons. The incorporation of a rapid microdialysis step implies that the data were recorded under nonequilibrium conditions, that is, while the zinc–protein complexes undergo dissociation in solution. Also, nonspecific binding (77) as well as dissociation (78) can occur during the ESI process. Nonetheless, the ESI-MS data in Figure 5 confirm a very strong binding preference of ProT α for Zn^{2+} compared to Ca^{2+} and Mg^{2+} .

This finding is also supported by the far-UV CD data in Figure 6. The prominent negative band centered around 198 nm clearly reflects the fact that ProT α remains extensively disordered under all conditions studied here (79). The addition of zinc reduces the intensity of this band by 17%. At the same time, spectral changes in the 210–230 nm region suggest a slightly increased α -helical propensity (blue line in Figure 6), consistent with the NMR data in Figure 3C. In contrast, virtually no changes in the CD spectrum are detectable upon the addition of Ca^{2+} or Mg^{2+} .

Pulsed-Field Gradient NMR Measurements. To study changes in the overall compactness of ProT α upon Zn^{2+} binding, PFG-NMR measurements (58) were carried out (Figure 7). In the absence of Zn^{2+} and NaCl, the ensemble-averaged hydrodynamic radius of the protein is $R_h = (33.7 \pm 0.3)$ Å. For a globular protein with the same number of residues as those of ProT α , R_h values of the native (R_h^N) and the fully denatured (R_h^D) states are predicted to be around 19 and 32 Å, respectively (59). The fact that the experimentally measured R_h value of ProT α is very close to R_h^D strongly suggests that the nonmetalated protein adopts an extended random coil structure. As the molar ratio of Zn^{2+} to ProT α is increased from 0 to 30 in the absence of NaCl, the R_h steadily decreases to (24.1 ± 0.4) Å, thus confirming the transition to more compact conformations (Figure 7A). In contrast, the addition of 3 mM of Ca^{2+} and Mg^{2+} only caused a very slight decrease in R_h from (33.7 ± 0.3) Å to (31.9 ± 0.7) Å and (32.7 ± 0.9) Å, respectively (data not shown).

Another way to represent these data employs the compaction factor, defined as $C = (R_h^D - R_h)/(R_h^D - R_h^N)$ (59), with $R_h^D = 33.7$ Å and $R_h^N = 18.6$ Å. Figure 7A shows that the compaction factor of ProT α increases from zero to (63.6

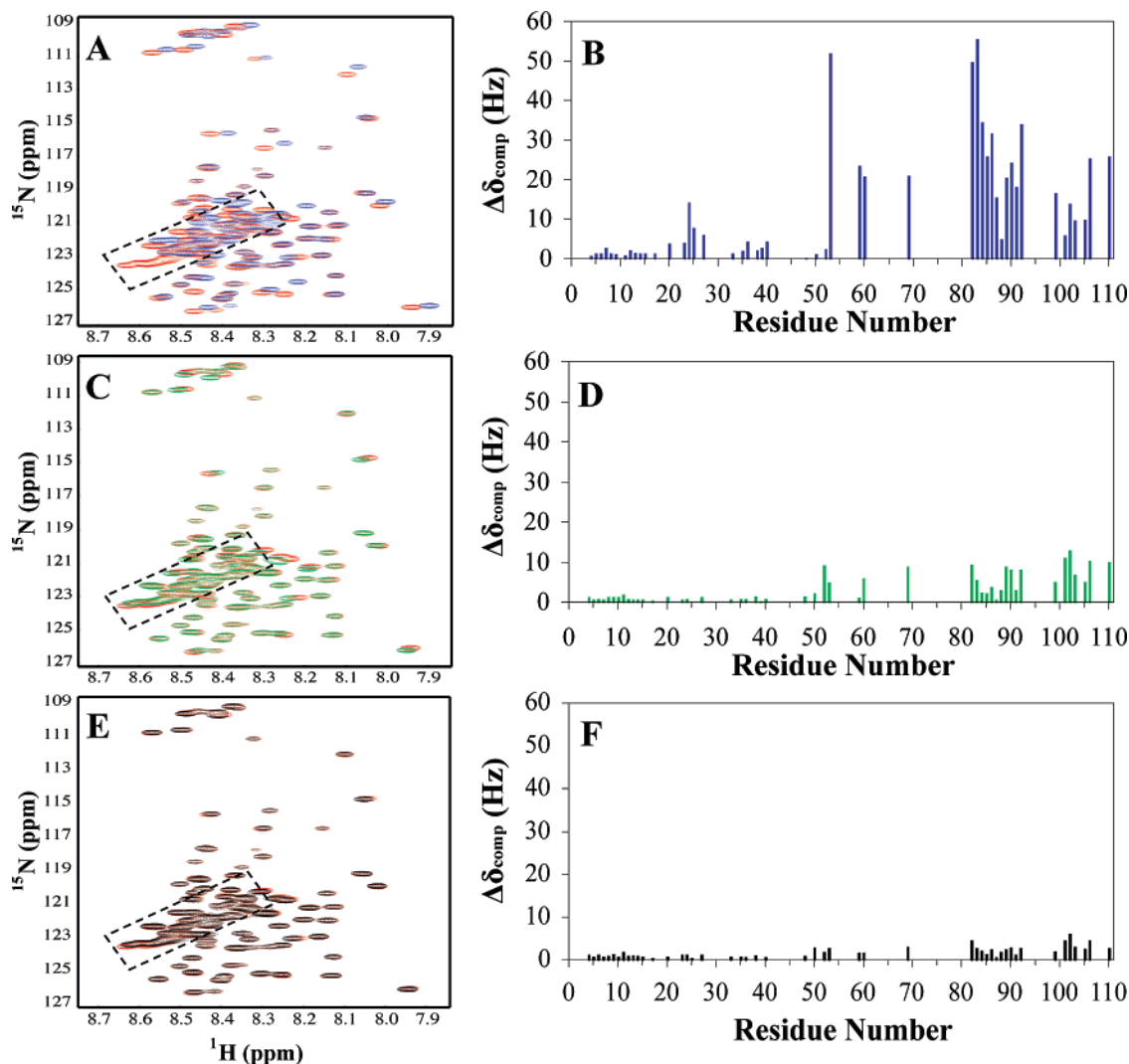


FIGURE 4: ^1H - ^{15}N HSQC spectra of ProT α in the presence and absence 3 mM ZnCl_2 (A), CaCl_2 (C), or MgCl_2 (E). Each sample contained 0.1 mM ^{15}N -labeled ProT α in 40 mM HEPES (pH 7.0) and 150 mM NaCl. Composite ^1H and ^{15}N chemical shift changes (in Hz) of ProT α upon interacting with Zn^{2+} (B), Ca^{2+} (D), and Mg^{2+} (F) in the presence of 150 mM NaCl are shown.

$\pm 2.6\%$) as the concentration of Zn^{2+} is raised from 0 to 3 mM. All R_i measurements were subsequently repeated in the presence of 150 mM NaCl. The observed trends in R_i and C upon zinc binding are very similar to those described above, even though the magnitude of the changes is somewhat reduced (Figure 7B). In the presence of 150 mM NaCl, changes in R_i upon addition of Ca^{2+} and Mg^{2+} are insignificant (data not shown).

Change in Backbone Dynamics upon Zinc-Binding. Backbone ^{15}N relaxation measurements are commonly used to study the residue-specific dynamic properties of proteins (80). ^{15}N R_1 , R_2 , and steady state ^1H - ^{15}N NOEs were measured using a 0.3 mM ^{15}N -labeled ProT α sample (Figure 8). Forty-nine assigned residues with well-resolved peaks in the ^1H - ^{15}N HSQC spectrum were used for this analysis. In the absence of Zn^{2+} , with the exception of D110 at the C-terminal end, all of the measured R_1 values of ProT α fall in a narrow range (1.2–2.0 s^{-1}), (Figure 8A, red). Upon the addition of 6 mM Zn^{2+} (blue), significant increases in R_1 were observed for residues 48–82, suggesting a reduction of picosecond–nanosecond motion in this region of the protein.

In the absence of Zn^{2+} (Figure 8B, red), the variation of R_2 values along the sequence is relatively small (2.3–4.2 s^{-1} , except that for D110). Upon binding to zinc (blue), significant changes are observed for residues 48–110, while the R_2 values of residues 4–40 remain largely unchanged. Since motions on nanosecond (segmental motions and molecular tumbling) and on micro to millisecond time scales (large-amplitude conformational transitions) both contribute to the observed R_2 values, we performed the ^{15}N relaxation dispersion experiments (with CPMG field strength ranging from 50 to 1000 Hz) in order to estimate the contributions of the latter (81, 82) (data not shown). No significant relaxation dispersion was observed for any of the backbone amide signals. This result suggests that the conformational exchange on the millisecond time scale does not contribute to the notable increase in R_2 for residues in the C-terminal portion (especially 48–82). However, contributions of transitions occurring on faster time scales cannot be excluded.

The steady state ^1H - ^{15}N NOE is sensitive to fast internal motions of the backbone, providing a good indicator of protein mobility on the picosecond–nanosecond time scale. For a folded protein with a molecular weight corresponding

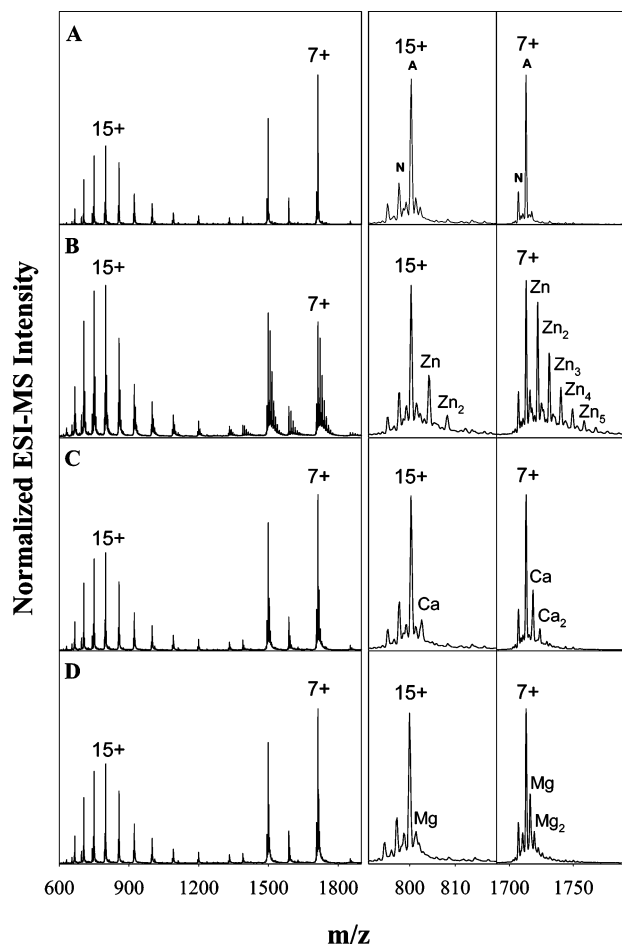


FIGURE 5: ESI mass spectra of ProT α recorded in the presence of 150 mM ammonium acetate and 3 mM of different metal cations. (A) No metals added [control]; (B) ZnCl₂; (C) CaCl₂; (D) MgCl₂. For panels B–D, the protein was subjected to rapid on-line dialysis immediately prior to ESI. Notation: Zn represents the protein bound to one zinc ion, and Zn₂ denotes two bound zinc ions, etc.

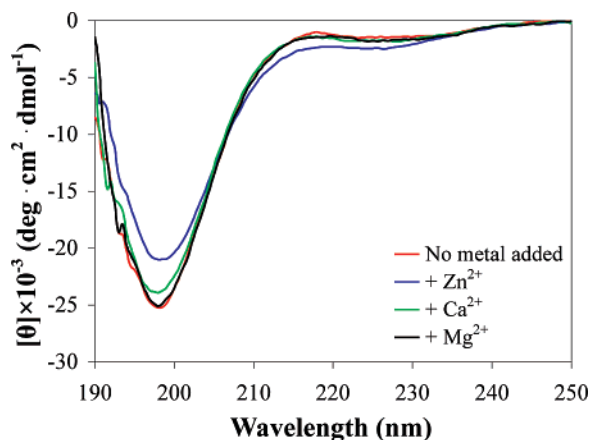


FIGURE 6: Circular dichroism spectra of ProT α in 150 mM NaCl recorded in the absence of divalent cations (red), with 3 mM ZnCl₂ (blue), CaCl₂ (green), or MgCl₂ (black).

to that of ProT α , the NOE values for residues with restricted mobility would be expected to be around 0.8 (83). A lower NOE value indicates an increased local flexibility. For residues in highly unstructured regions, the NOE values are generally strongly negative. In the absence of Zn²⁺ (Figure 8C, red), the NOE values for ProT α are predominantly negative, which is consistent with the highly unstructured

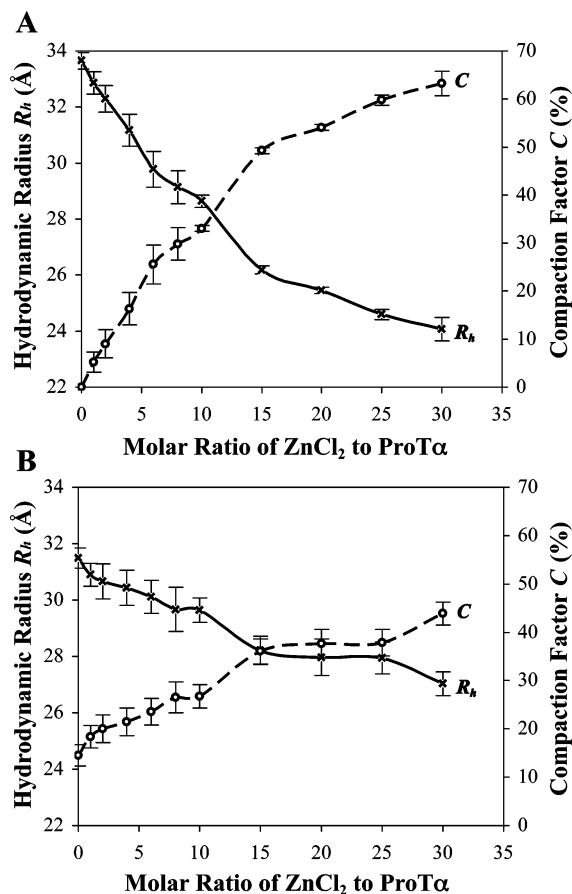


FIGURE 7: Hydrodynamic radius (\times) of ProT α in the presence of different molar ratios of Zn²⁺ measured by PFG-NMR. Measurements were performed with 0 mM NaCl (A) or 150 mM NaCl (B). Compaction factor (O) was determined as described by Wilkins et al. (40).

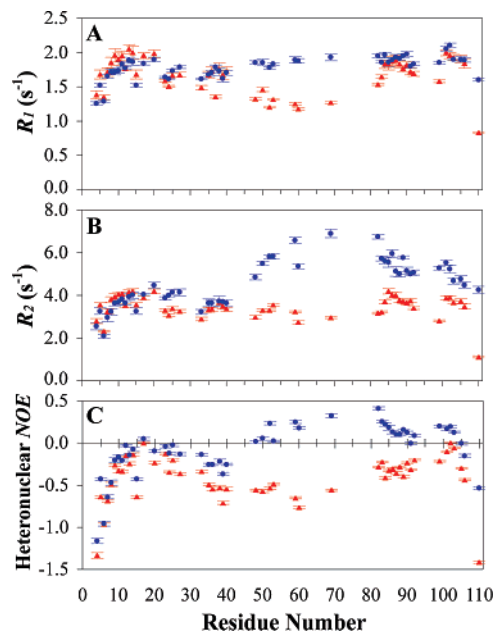


FIGURE 8: Backbone ¹⁵N relaxation measurements of ProT α . The experiments were carried out in the presence (blue) and absence (red) of 6 mM ZnCl₂. (A) Longitudinal relaxation rate (R_1); (B) transverse relaxation rate (R_2); and (C) steady-state ¹H-¹⁵N NOE.

nature of the protein. Upon the addition of Zn²⁺ (blue), however, positive NOE values were observed for residues 48–103, while the NOE values for the residues in the

N-terminal portion (residues 4–40) remain negative. Figure S1A and B (Supporting Information) show the ^1H - ^{15}N NOE spectra (with ^1H saturation) of ProTα in the absence and the presence of Zn^{2+} , respectively. Most of the signals in the dashed box in Figure S1B (Supporting Information) are positive, suggesting that many of the unassigned acidic residues in GRR display a restricted mobility upon binding to Zn^{2+} .

To further analyze the measured relaxation parameters, reduced spectral density mapping was performed to determine the contributions of motions occurring at different frequencies to the relaxation processes (63, 84). The spectral density function values of NH vectors at three specific frequencies, 0, $61(\omega_N)$, and $521(0.87\omega_H)$ MHz, were determined (Figure S2, Supporting Information). Similar to what we observed for the R_2 and NOE values, notable changes in spectral density function values were observed for residues 48–82 upon the addition of Zn^{2+} (blue), especially at the zero frequency. Since $J(0)$ is directly related to the correlation times associated with internal motions occurring in the nanosecond range as well as the overall tumbling of the protein (84), the result suggests that the rotational fluctuations of the NH vectors in this region become more restricted upon binding to zinc.

DISCUSSION

Although ProTα can bind to multiple protein targets, very little structural information on this protein has been available so far (50, 85), thereby impeding progress in understanding its function. In this work, we used NMR spectroscopy and ESI-MS to characterize the structure and dynamics of ProTα and its interaction with zinc ions. A detailed chemical shift analysis confirms the intrinsically disordered character of nonmetalated ProTα under physiological conditions, with only a slight propensity for β -strand structure. This result is compatible with the R_h measurements, which confirm that ProTα is extensively unfolded in the absence of zinc.

On the basis of chemical shift mapping, we delineated the zinc-binding region of ProTα (50, 85). Unlike typical zinc-binding proteins, which use Cys and His for metal coordination, it seems that ProTα interacts with zinc via the carboxyl groups of its Glu and Asp (50, 85). This work has uncovered that ProTα specifically binds to Zn^{2+} via its C-terminal portion (residues 48–110), which includes a long glutamic acid-rich stretch. This part of the protein undergoes partial folding upon metal binding. The results of previous studies estimated that the apparent K_d for zinc-binding to ProTα is in the range of $100\ \mu\text{M}$ – $1\ \text{mM}$ (50, 85). Since the exact number of zinc binding sites on ProTα still remains unknown, site-specific dissociation constants cannot be determined accurately. The amide ^1H and ^{15}N chemical shift changes measured here are consistent with an apparent K_d on the order of $1\ \text{mM}$. It should be noted that this value is a weighted average for the possibly multiple binding sites. Also, since many of the resonance signals that are most affected by zinc binding are unassigned, the apparent K_d may be overestimated.

Ample examples have shown that intrinsically disordered proteins undergo disorder-to-order transitions upon binding to their targets (86). The large entropic penalties for these transitions render the interactions low in affinity yet high in

specificity, which may be crucial for their roles in cellular regulation processes (86). For some disordered proteins, the strategy being employed to reduce the entropic penalty upon binding is to interact with targets via transiently formed secondary structure elements (17). Since the structure of nonmetalated ProTα has been shown to be highly flexible and extensively unfolded, it is unlikely that the protein interacts with its targets through preformed structural elements. Therefore, the target-binding affinities of apo-ProTα are weak (36).

On the basis of the result of R_h and chemical shift measurements, ProTα undergoes significant conformational changes and collapses into compact conformations upon zinc binding. The results of backbone relaxation measurements clearly indicate that the flexibility of the GRR in this compact state is greatly reduced. From a thermodynamic point of view, the binding of ProTα to its targets via this zinc-induced partially folded state will likely have a lower entropic penalty, thereby rendering the protein–protein interaction more favorable. We thus propose that the cellular level of Zn^{2+} may act as a switch that controls the function of ProTα by substantially changing the free-energy landscape of its interaction with target proteins.

For instance, apo-ProTα binds only weakly to Keap1. The interaction between these two proteins, however, is significantly enhanced in the presence of zinc (36), allowing ProTα to compete with the Neh2 domain of Nrf2 for binding to Keap1. The results of this work, combined with those of previous studies (36, 87), provide insights into how zinc binding can provide a way to enhance the interaction between ProTα and its targets. NMR studies have demonstrated that the 98-residue Neh2 domain of Nrf2 is partially disordered and that the Keap1-binding ETGE motif is located next to a well-defined 33-residue central helical region of that protein (87). The proximity to a structured segment may restrict the mobility of residues in the ETGE motif as suggested by their very small heteronuclear NOE values. On the other hand, pull-down experiments indicate that residues 32–52 of ProTα are involved in binding to Keap1 (36). This 21-residue Keap1 binding-site of ProTα is located N-terminal to the GRR. The results of our chemical shift analysis and backbone relaxation studies demonstrate that zinc binding to the GRR can induce a significant reduction in dynamics of the Keap1-binding site of ProTα (Figure 8). This may reduce the entropic penalty for ProTα upon binding to Keap1. Further investigations on the thermodynamics of binding ProTα to Keap1 are needed to verify this hypothesis.

A multitude of examples has demonstrated that the function of disordered proteins can be closely related to their metal-binding properties. For instance, the binding of Cu^{2+} to the unstructured octarepeat domain in the N-terminal region of prion protein may play a crucial role in amyloid formation (88). Similarly, metal ions such as Al^{3+} , Cu^{2+} , Fe^{3+} , Co^{3+} , and Mn^{2+} can accelerate fibrillation of α -synuclein (89). It has also been shown that Zn^{2+} can bind to the unstructured N-terminal domain of HIV-1 integrase to induce the tetramerization of the protein and enhance its catalytic activity (90). Therefore, the reduction in plasticity and/or conformational changes upon metal-binding may represent a general mechanism for enhancing the target recognition of intrinsically disordered proteins.

ACKNOWLEDGMENT

We thank Dr. Andrey Vartapetian (University of Moscow) for providing the ProT α expression plasmid.

SUPPORTING INFORMATION AVAILABLE

¹H-¹⁵N NOE spectra (with ¹H saturation) of ProT α in the absence and the presence of 20 molar equiv of Zn²⁺ (Figure S1) and the results of reduced spectral density analysis (Figure S2). This material is available free of charge via the Internet at <http://pubs.acs.org>.

REFERENCES

- Wright, P. E., and Dyson, H. J. (1999) Intrinsically unstructured proteins: Re-assessing the protein structure-function paradigm, *J. Mol. Biol.* **293**, 321–331.
- Dunker, A. K., Lawson, J. D., Brown, C. J., Williams, R. M., Romero, P., Oh, J. S., Oldfield, C. J., Campen, A. M., Ratliff, C. M., Hipps, K. W., Ausio, J., Nissen, M. S., Reeves, R., Kang, C. H., Kissinger, C. R., Bailey, R. W., Griswold, M. D., Chiu, W., Garber, E. C., and Obradovic, Z. (2001) Intrinsically disordered proteins, *J. Mol. Graphics Modell.* **19**, 26–59.
- Tompa, P. (2002) Intrinsically unstructured proteins, *Trends Biochem. Sci.* **27**, 527–533.
- Dyson, H. J., and Wright, P. E. (2005) Intrinsically unstructured proteins and their functions, *Nat. Rev. Mol. Cell. Biol.* **6**, 197–208.
- Tompa, P. (2005) The interplay between structure and function in intrinsically unstructured proteins, *FEBS Lett.* **579**, 3346–3354.
- Ward, J. J., Sodhi, J. S., McGuffin, L. J., Buxton, B. F., and Jones, D. T. (2004) Prediction and functional analysis of native disorder in proteins from the three kingdoms of life, *J. Mol. Biol.* **337**, 635–645.
- Iakoucheva, L. M., Brown, C. J., Lawson, J. D., Obradovic, Z., and Dunker, A. K. (2002) Intrinsic disorder in cell-signaling and cancer-associated proteins, *J. Mol. Biol.* **323**, 573–584.
- Cheng, Y., LeGall, T., Oldfield, C. J., Dunker, A. K., and Uversky, V. N. (2006) Abundance of intrinsic disorder in protein associated with cardiovascular disease, *Biochemistry* **45**, 10448–10460.
- Minezaki, Y., Homma, K., Kinjo, A. R., and Nishikawa, K. (2006) Human transcription factors contain a high fraction of intrinsically disordered regions essential for transcriptional regulation, *J. Mol. Biol.* **359**, 1137–1149.
- Cheng, Y., LeGall, T., Oldfield, C. J., Mueller, J. P., Van, Y.-Y., J., Romero, P., Cortese, M. S., Uversky, V. N., and Dunker, A. K. (2006) Rational drug design via intrinsically disordered protein, *Trends Biotechnol.* **24**, 435–442.
- Dyson, H. J., and Wright, P. E. (2001) Nuclear magnetic resonance methods for elucidation of structure and dynamics in disordered states, *Methods Enzymol.* **339**, 258–270.
- Dyson, H. J., and Wright, P. E. (2005) Elucidation of the protein folding landscape by NMR, *Methods Enzymol.* **394**, 299–321.
- Mittag, T., and Forman-Kay, J. D. (2007) Atomic-level characterization of disordered protein ensembles, *Curr. Opin. Struct. Biol.* **17**, 3–14.
- Galea, C. A., Pagala, V. R., Obenauer, J. C., Park, C. G., Slaughter, C. A., and Kriwacki, R. W. (2006) Proteomic studies of the intrinsically unstructured mammalian proteome, *J. Proteome Res.* **5**, 2839–2848.
- Csizmok, V., Dosztanyi, Z., Simon, I., and Tompa, P. (2007) Towards proteomic approaches for the identification of structural disorder, *Curr. Protein Pept. Sci.* **8**, 173–179.
- Choy, W. Y., and Forman-Kay, J. D. (2001) Calculation of ensembles of structures representing the unfolded state of an SH3 domain, *J. Mol. Biol.* **308**, 1011–1032.
- Fuxreiter, M., Simon, I., Friedrich, P., and Tompa, P. (2004) Preformed structural elements feature in partner recognition by intrinsically unstructured proteins, *J. Mol. Biol.* **338**, 1015–1026.
- Mohan, A., Oldfield, C. J., Radivojac, P., Vacic, V., Cortese, M. S., Dunker, A. K., and Uversky, V. N. (2006) Analysis of molecular recognition features (MoRFs), *J. Mol. Biol.* **362**, 1043–1059.
- Tompa, P., Szasz, C., and Buday, L. (2005) Structural disorder throws new light on moonlighting, *Trends Biochem. Sci.* **30**, 484–489.
- Fuxreiter, M., Tompa, P., and Simon, I. (2007) Local structural disorder imparts plasticity on linear motifs, *Bioinformatics* **23**, 950–956.
- Dunker, A. K., Cortese, M. S., Romero, P., Iakoucheva, L. M., and Uversky, V. N. (2005) Flexible nets: The roles of intrinsic disorder in protein interaction networks, *FEBS J.* **272**, 5129–5148.
- Ma, B., Shatsky, M., Wolfson, H. J., and Nussinov, R. (2002) Multiple diverse ligands binding at a single protein site: A matter of pre-existing populations, *Protein Sci.* **11**, 184–197.
- Bracken, C. (2001) NMR spin relaxation methods for characterization of disorder and folding in proteins, *J. Mol. Graphics Modell.* **19**, 3–12.
- Garcia, P., Serrano, L., Durand, D., Rico, M., and Bruix, M. (2001) NMR and SAXS characterization of the denatured state of the chemotactic protein cheY: Implications for protein folding initiation, *Protein Sci.* **10**, 1100–1112.
- Dyson, H. J., and Wright, P. E. (2004) Unfolded proteins and protein folding studied by NMR, *Chem. Rev.* **104**, 3607–3622.
- Lacy, E. R., Filippov, I., Lewis, W. S., Otieno, S., Xiao, L., Weiss, S., Hengst, L., and Kriwacki, R. W. (2004) p27 binds cyclin-cdk complexes through a sequential mechanism involving binding-induced protein folding, *Nat. Struct. Mol. Biol.* **11**, 358–364.
- Sugae, K., Dyson, H. J., and Wright, P. E. (2007) Mechanism of coupled folding and binding of an intrinsically disordered protein, *Nature* **447**, 1021–1025.
- Haritos, A. A., Goodall, G. J., and Horecker, B. L. (1984) Prothymosin α : Isolation and properties of the major immunoreactive form of thymosin α 1 in rat thymus, *Proc. Natl. Acad. Sci. U.S.A.* **81**, 1008–1011.
- Pineiro, A., Cordero, O. J., and Nogueira, M. (2000) Fifteen years of prothymosin α : Contradictory past and new horizons, *Peptides* **21**, 1433–1446.
- Segade, F., and Gomez-Marquez, J. (1999) Prothymosin α , *Int. J. Biochem. Cell Biol.* **31**, 1243–1248.
- Letsas, K. P., and Frangou-Lazaridis, M. (2006) Surfing on prothymosin α proliferation and anti-apoptotic properties, *Neoplasia* **53**, 92–96.
- Papamarcaki, T., and Tsolas, O. (1994) Prothymosin α binds to histone H1 in vitro, *FEBS Lett.* **345**, 71–75.
- Karetsou, Z., Sandaltzopoulos, R., Frangou-Lazaridis, M., Lai, C. Y., Tsolas, O., Becker, P. B., and Papamarcaki, T. (1998) Prothymosin α modulates the interaction of histone H1 with chromatin, *Nucleic Acids Res.* **26**, 3111–3118.
- Karetsou, Z., Kretsovali, A., Murphy, C., Tsolas, O., and Papamarcaki, T. (2002) Prothymosin α interacts with the CREB-binding protein and potentiates transcription, *EMBO Rep.* **3**, 361–366.
- Karetsou, Z., Martic, G., Tavoulari, S., Christoforidis, S., Wilm, M., Gruss, C., and Papamarcaki, T. (2004) Prothymosin α associates with the oncoprotein SET and is involved in chromatin decondensation, *FEBS Lett.* **577**, 496–500.
- Karapetian, R. N., Evstafieva, A. G., Abaeva, I. S., Chichkova, N. V., Filonov, G. S., Rubtsov, Y. P., Sukhacheva, E. A., Melnikov, S. V., Schneider, U., Wanker, E. E., and Vartapetian, A. B. (2005) Nuclear oncoprotein prothymosin α is a partner of Keap1: Implications for expression of oxidative stress-protecting genes, *Mol. Cell. Biol.* **25**, 1089–1099.
- Itoh, K., Chiba, T., Takahashi, S., Ishii, T., Igarashi, K., Katoh, Y., Oyake, T., Hayashi, N., Satoh, K., Hatayama, I., Yamamoto, M., and Nabeshima, Y. (1997) An Nrf2/small maf heterodimer mediates the induction of phase II detoxifying enzyme genes through antioxidant response elements, *Biochem. Biophys. Res. Commun.* **236**, 313–322.
- McMahon, M., Itoh, K., Yamamoto, M., and Hayes, J. D. (2003) Keap1-dependent proteasomal degradation of transcription factor Nrf2 contributes to the negative regulation of antioxidant response element-driven gene expression, *J. Biol. Chem.* **278**, 21592–21600.
- Goldstein, J. C., Waterhouse, N. J., Juin, P., Evan, G. I., and Green, D. R. (2000) The coordinate release of cytochrome *c* during apoptosis is rapid, complete and kinetically invariant, *Nat. Cell Biol.* **2**, 156–162.
- Wang, X. (2001) The expanding role of mitochondria in apoptosis, *Genes Dev.* **15**, 2922–2933.
- Acehan, D., Jiang, X., Morgan, D. G., Heuser, J. E., Wang, X., and Akey, C. W. (2002) Three-dimensional structure of the

- apoptosome: Implications for assembly, procaspase-9 binding, and activation, *Mol. Cell* 9, 423–432.
42. Adams, J. M., and Cory, S. (2002) Apoptosomes: Engines for caspase activation, *Curr. Opin. Cell Biol.* 14, 715–720.
43. Jiang, X., and Wang, X. (2000) Cytochrome *c* promotes caspase-9 activation by inducing nucleotide binding to Apaf-1, *J. Biol. Chem.* 275, 31199–31203.
44. Shi, Y. (2002) Apoptosome: The cellular engine for the activation of caspase-9, *Structure* 10, 285–288.
45. Jiang, X., Kim, H., Shu, H., Zhao, Y., Zhang, H., Kofron, J., Donnelly, J., Burns, D., Ng, S., Rosenberg, S., and Wang, X. (2003) Distinctive roles of PHAP proteins and prothymosin- α in a death regulatory pathway, *Nature* 299, 223–226.
46. Markova, O. V., Evstafieva, A. G., Mansurova, S. E., Moussine, S. S., Palamarchuk, L. A., Pereverzev, M. O., Vartapetian, A. B., and Skulachev, V. P. (2003) Cytochrome *c* is transformed from anti- to pro-oxidant when interacting with truncated oncoprotein prothymosin α , *Biochim. Biophys. Acta* 1557, 109–117.
47. Gast, K., Damaschun, H., Eckert, K., Schulze-Forster, K., Maurer, H. R., Muller-Frohne, M., Zirwer, D., Czarnecki, J., and Damaschun, G. (1995) Prothymosin α : A biologically active protein with random coil conformation, *Biochemistry* 34, 13211–13218.
48. Uversky, V. N., Gillespie, J. R., Millett, I. S., Khodyakova, A. V., Vasiliev, A. M., Chernovskaya, T. V., Vasilenko, R. N., Kozlovskaya, G. D., Dolgikh, D. A., Fink, A. L., Doniach, S., and Abramov, V. M. (1999) Natively unfolded human prothymosin α adopts partially folded collapsed conformation at acidic pH, *Biochemistry* 38, 15009–15016.
49. Uversky, V. N., Gillespie, J. R., and Fink, A. L. (2000) Why are “natively unfolded” proteins unstructured under physiologic conditions, *Proteins* 41, 415–427.
50. Chichkova, N. V., Evstafieva, A. G., Lyakhov, I. G., Tsvetkov, A. S., Smirnova, T. A., Karapetian, R. N., Karger, E. M., and Vartapetian, A. B. (2000) Divalent metal cation binding properties of human prothymosin α , *Eur. J. Biochem.* 267, 4745–4752.
51. Evstafieva, A. G., Chichkova, N. V., Makarova, T. N., Vartapetian, A. B., Vasilenko, A. V., Abramov, V. M., and Bogdanov, A. A. (1995) Overproduction in *Escherichia coli*, purification and properties of human prothymosin α , *Eur. J. Biochem.* 231, 639–643.
52. Yi, S., Brickenden, A., and Choy, W. Y. (2007) A new protocol for high-yield purification of recombinant human prothymosin α expressed in *Escherichia coli* for NMR studies, *Protein Expression Purif.*, in press.
53. Kalthoff, C. (2003) A novel strategy for the purification of recombinantly expressed unstructured protein domains, *J. Chromatogr., B* 786, 247–254.
54. Wishart, D. S., Bigam, C. G., Yao, J., Abildgaard, F., Dyson, H. J., Markley, J. L., and Sykes, B. D. (1995) ^1H , ^{13}C , ^{15}N chemical shift referencing in biomolecular NMR, *J. Biomol. NMR* 6, 135–140.
55. Delaglio, F., Grzesiek, S., Vuister, G. W., Zhu, G., Pfeifer, J., and Bax, A. (1995) NMRPIPE: A multidimensional spectral processing system based on UNIX pipes, *J. Biomol. NMR* 6, 277–293.
56. Johnson, B. A. (2004) Using NMRView to visualize and analyze the NMR spectra of macromolecules, *Methods Mol. Biol.* 278, 313–352.
57. Sattler, M., Schleucher, J., and Griesinger, C. (1999) Heteronuclear multidimensional NMR experiments for the structure determination of proteins in solution employing pulsed field gradients, *Prog. Nucl. Magn. Reson. Spectrosc.* 34, 93–158.
58. Altieri, A. S., Hinton, D. P., and Byrd, R. A. (1995) Association of biomolecular systems via pulsed field gradient NMR self-diffusion measurements, *J. Am. Chem. Soc.* 117, 7566–7567.
59. Wilkins, D. K., Grimshaw, S. B., Receveur, V., Dobson, C. M., Jones, J. A., and Smith, L. J. (1999) Hydrodynamic radii of native and denatured proteins measured by pulse field gradient NMR techniques, *Biochemistry* 38, 16424–16431.
60. Akke, M., and Palmer, A. G. (1996) Monitoring macromolecular motions on microsecond-millisecond time scales by $R_{1\rho}$ and R_1 constant relaxation time NMR spectroscopy, *J. Am. Chem. Soc.* 118, 911–912.
61. Farrow, N. A., Muhandiram, R., Singer, A. U., Pascal, S. M., Kay, C. M., Gish, G., Shoelson, S. E., Pawson, T., Forman-Kay, J. D., and Kay, L. E. (1994) Backbone dynamics of a free and phosphopeptide-complexed Src homology 2 domain studied by ^{15}N NMR relaxation, *Biochemistry* 33, 5984–6003.
62. Davis, D. G., Perlman, M. E., and London, R. E. (1994) Direct measurements of the dissociation-rate constant for inhibitor-enzyme complexes via the T1 rho and T2 (CPMG) methods, *J. Magn. Reson., Ser. B* 104, 266–275.
63. Farrow, N. A., Zhang, O., Szabo, A., Torchia, D. A., and Kay, L. E. (1995) Spectral density function mapping using ^{15}N relaxation data exclusively, *J. Biomol. NMR* 6, 153–162.
64. Xu, N., Lin, Y., Hofstadler, S. A., Matson, D., Call, C. J., and Smith, R. D. (1998) A microfabricated dialysis device for sample cleanup in electrospray ionization mass spectrometry, *Anal. Chem.* 70, 3553–3556.
65. Benkestock, K., Edlund, P. O., and Roeraade, J. (2002) On-line microdialysis for enhanced resolution and sensitivity during electrospray mass spectrometry of non-covalent complexes and competitive binding studies, *Rapid Commun. Mass Spectrom.* 16, 2054–2059.
66. Spera, S., and Bax, A. (1991) Empirical correlation between protein backbone conformation and $\text{C}\alpha$ and $\text{C}\beta$ ^{13}C nuclear magnetic resonance chemical shifts, *J. Am. Chem. Soc.* 113, 5490–5492.
67. Wang, L., Eghbalnia, H. R., Bahrami, A., and Markley, J. L. (2005) Linear analysis of carbon-13 chemical shift differences and its application to the detection and correction of errors in referencing and spin system identifications, *J. Biomol. NMR* 32, 13–22.
68. Wishart, D. S., and Sykes, B. D. (1994) The ^{13}C chemical-shift index: A simple method for the identification of protein secondary structure using ^{13}C chemical-shift data, *J. Biomol. NMR* 4, 171–180.
69. Babu, K. R., and Douglas, D. J. (2000) Methanol-induced conformations of myoglobin at pH 4.0, *Biochemistry* 39, 14702–14710.
70. Invernizzi, G., Samalikova, M., Brocca, S., Lotti, M., Molinari, H., and Grandori, R. (2006) Comparison of bovine and porcine β -lactoglobulin: A mass spectrometric analysis, *J. Mass Spectrom.* 41, 717–727.
71. Konermann, L., and Holzwarth, A. R. (1996) Analysis of the absorption spectrum of photosystem II reaction centers: Temperature dependence, pigment assignment, and inhomogeneous broadening, *Biochemistry* 35, 829–842.
72. Wagner, D. S., and Anderegg, R. J. (1994) Conformation or cytochrome *c* studied by deuterium exchange-electrospray ionization mass spectrometry, *Anal. Chem.* 66, 706–711.
73. Kaltashov, I. A., and Eyles, S. J. (2005) Mass Spectrometry, in *Biophysics*, John Wiley and Sons Inc., Hoboken, NJ.
74. Konermann, L. (2007) A minimalist model for exploring conformational effects on the electrospray charge state distribution of proteins, *J. Phys. Chem. B* 111, 6534–6543.
75. Kuprowski, M. C., Boys, B. L., and Konermann, L. (2007) Analysis of protein mixtures by electrospray mass spectrometry: Effects of conformation and desolvation behavior on the signal intensities of hemoglobin subunits, *J. Am. Soc. Mass Spectrom.* 18, 1279–1285.
76. Kuprowski, M. C., and Konermann, L. (2007) Signal response of co-existing protein conformers in electrospray mass spectrometry, *Anal. Chem.* 79, 2499–2506.
77. Hu, P. F., Ye, Q. Z., and Loo, J. A. (1994) Calcium stoichiometry determination for calcium binding proteins by electrospray ionization mass spectrometry, *Anal. Chem.* 66, 4190–4194.
78. Iavarone, A. T., Udekwu, O. A., and Williams, E. R. (2004) Buffer loading for counteracting metal salt-induced signal suppression in electrospray ionization, *Anal. Chem.* 76, 3944–3950.
79. Greenfield, N., and Fasman, G. D. (1969) Computed circular dichroism spectra for the evaluation of protein conformation, *Biochemistry* 8, 4108–4116.
80. Kay, L. E. (1998) Protein dynamics from NMR, *Nat. Struct. Biol.* 5, 513–517.
81. Choy, W. Y., Zhou, Z., Bai, Y., and Kay, L. E. (2005) An ^{15}N NMR spin relaxation dispersion study of the folding of a pair of engineered mutants of apocytochrome *b*₅₆₂, *J. Am. Chem. Soc.* 127, 5066–5072.
82. Loria, J. P., Rance, M., and Palmer, A. G. (1999) A relaxation-compensated Carr-Purcell-Meiboom-Gill sequence for characterizing chemical exchange by NMR spectroscopy, *J. Am. Chem. Soc.* 121, 2331–2332.
83. Alexandrescu, A. T., and Shortle, D. (1994) Backbone dynamics of a highly disordered 131 residue fragment of staphylococcal nuclease, *J. Mol. Biol.* 242, 527–546.
84. Peng, J. W., and Wagner, G. (1992) Mapping of the spectral densities of N-H bond motions in Eglin c using heteronuclear relaxation experiments, *Biochemistry* 31, 8571–8576.

85. Uversky, V. N., Gillespie, J. R., Millett, I. S., Khodyakova, A. V., Vasilenko, R. N., Vasiliev, A. M., Rodionov, I. L., Kozlovskaya, G. D., Dolgikh, D. A., Fink, A. L., Doniach, S., Permyakov, E. A., and Abramov, V. M. (2000) Zn²⁺-mediated structure formation and compaction of the "natively unfolded" human prothymosin α , *Biochem. Biophys. Res. Commun.* 267, 663–668.
86. Dyson, H. J., and Wright, P. E. (2002) Coupling of folding and binding for unstructured proteins, *Curr. Opin. Struct. Biol.* 12, 54–60.
87. Tong, K. I., Kato, Y., Kusunoki, H., Itoh, K., Tanaka, T., and Yamamoto, M. (2006) Keap1 recruits Neh2 through binding to ETGE and DLG motifs: Characterization of the two-site molecular recognition model, *Mol. Cell. Biol.* 26, 2887–2900.
88. Millhauser, G. L. (2007) Copper and the prion protein: Methods, structures, function, and disease, *Annu. Rev. Phys. Chem.* 58, 299–320.
89. Uversky, V. N., Li, J., and Fink, A. L. (2001) Metal-triggered structural transformations, aggregation, and fibrillation of human α -synuclein. A possible molecular link between parkinson's disease and heavy metal exposure, *J. Biol. Chem.* 276, 44284–44296.
90. Zheng, R., Jenkins, T. M., and Craigie, R. (1996) Zinc folds the N-terminal domain of HIV-1 integrase, promotes multimerization, and enhances catalytic activity, *Proc. Natl. Acad. Sci. U.S.A.* 93, 13659–13664.

BI7014822